Dust Emission and Star Formation Activities of High Redshift Weak Emission Line Quasars

Zile Zeng

Mathematics and Science Academy, Fort Hays State University, Hays, USA
Email: z_zeng@mail.fhsu.edu (Z.L.Z.)
Manuscript received October 2, 2025; accepted December 7, 2025; published February 5, 2026.

***Abstract*—We present the work using the high-quality optically-selected quasar catalogue from the Sloan Digital Sky Survey (SDSS) to select a large sample of Weak Emission Line Quasars (WELQs). The Equivalent Widths (EWs) of their emission lines are on the weaker end of the spectrum for Active Galactic Nuclei (AGNs). Yet, their bolometric luminosity distribution is similar to that of Normal Emission Line Quasars (NELQs). By integrating data from multiple wavelength bands, including the ultraviolet data from the Galaxy Evolution Explorer (GALEX), the near-infrared data from the United Kingdom Infrared Telescope Deep Sky Survey (UKIDSS), the mid-infrared data from the Wide-field Infrared Survey Explorer (WISE), and the far-infrared images from the Herschel Space Telescope, we conducted a comprehensive study on the Spectral Energy Distribution (SED) of WELQs across ultraviolet, optical, near-infrared, mid-infrared, and far-infrared bands. Our research indicates that within the redshift range of $1<z<3$, the average far-infrared luminosity of WELQs is approximately 5-10 times higher than that of normal quasars, with no significant evolution with redshift. This suggests that WELQs may be characterised by intense star formation activities in their host galaxies, heating the surrounding dust, and potentially being in an early evolutionary stage of AGNs. The underdeveloped Broad Emission Line Region (BELR) and Narrow Emission Line Region (NELR) might contribute to their weak emission lines. Further data processing and upcoming survey projects are expected to unveil the physical origins of WELQs, enhancing our understanding of the formation and evolution of quasars and AGNs.**

***Keywords*—Weak Emission Line Quasars (WELQs), spectral energy distribution, active galactic nuclei**

I. Introduction

Active Galactic Nuclei (AGN) are the central region of the active galaxies in the Universe that have extremely high energy radiation across broad bands of the electromagnetic spectrum, covering from low-frequency radio wavelengths to high-frequency X-rays. A rapidly accreting supermassive black hole is believed to exist at the center of AGN. The matter around the black hole is accreted by extremely intensive gravity, thus forming the accretion disk and transferring the gravitational energy into electromagnetic radiation energy. The AGN is a crucial evolutionary stage of galaxies. Therefore, plenty of work has been devoted to understanding the nature of AGN and its interplay with star formation activities in the host galaxies via strong AGN feedback.

A. Fundamentals of Observational Astronomy

The radiation power of the given celestial object is defined as the total radiated energy during the unit time, referred to as bolometric luminosity; then, we have

$$L = \frac{dE}{dt}. \tag{1}$$

Radiation power in the infinitesimal interval of frequency $(\nu, \nu + \mathrm{d}\nu)$ or wavelength $(\lambda, \lambda + \mathrm{d}\lambda)$ is called monochromatic luminosity, expressed as

$$L_\nu = \frac{dE}{dt\, d\nu}, \tag{2}$$

$$L_\lambda = \frac{dE}{dt\, d\lambda}. \tag{3}$$

The flux density describes the radiation energy of the celestial object received via the detector, expressed as

$$f_\nu = \frac{dE}{dt\, d\nu\, dA} = \frac{L_\nu}{4\pi d_L^2}, \tag{4}$$

$$f_\nu = \frac{dE}{dt\, d\lambda\, dA} = \frac{L_\lambda}{4\pi d_L^2}. \tag{5}$$

For specific wave band X. Through calibrating the flux density zero point of telescope system $f^*_{\nu,\mathrm{X}}$ and $f^*_{\lambda,\mathrm{X}}$, The Apparent Magnitude can be expressed as

$$m_X = -2.5log_{10}\frac{f_{\nu,X}}{f^*_{\nu,X}} = -2.5log_{10}\frac{f_{\lambda,X}}{f^*_{\lambda,X}} \tag{6}$$

The luminosity can be expressed by its absolute magnitude. The relation between luminosity and apparent magnitude can be described as

$$m_X - M_X = 5log_{10}\frac{d_L}{pc} - 5 \tag{7}$$

Here, parsec is defined as $1\mathrm{pc}=3.0857\times10^{16}$ m. For imaging observation, we can use photometric analysis to obtain the luminosity information for celestial objects. Besides that, spectroscopic observation is another powerful method to shed light on the physical information of distant celestial objects. The main features of spectra can be divided into a continuum, emission line, and absorption line, produced via continuous or discrete atomic energy level transitions. Therefore, we can use the spectrum further to understand the physical status of the celestial bodies. Usually, we describe the strength of spectral line and emission by equivalent width.

$$EW = \int_0^\infty \left(\frac{f_\lambda}{f_\lambda^c} - 1\right) d\lambda \tag{8}$$

Here, f_λ^{c} represents the continuum spectrum's flux density. When the substances that produce celestial radiation make microscopic motion, the wavelength and frequency will be influenced by it and form the Redshift and blue shift in the spectrum. So, it can refer to

DOI: 10.7763/IJET.2026.V18.1335

$$1 + z = \frac{\lambda}{\lambda_0} = \frac{\nu_0}{\nu} \quad (9)$$

The frequency shift in the spectrum can result from the inherited motion of a substance or the expansion of the cosmological spacetime, also known as cosmological Redshift. Therefore, the Redshift in cosmology also reflects its cosmic age and the distance between it and observers.

B. Formation and Transaction of Galaxy

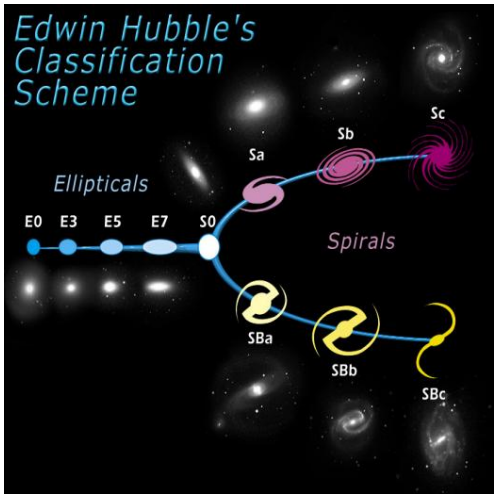

(a)

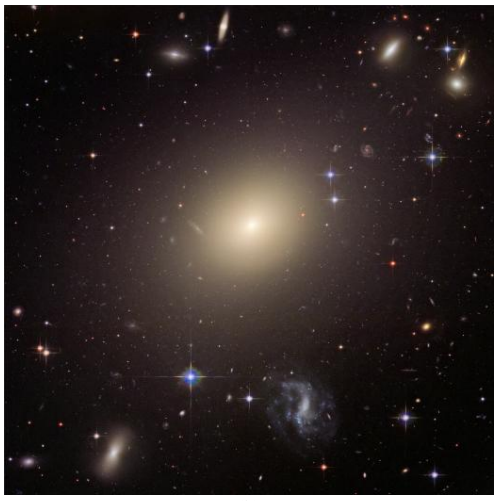

(b)

(c)

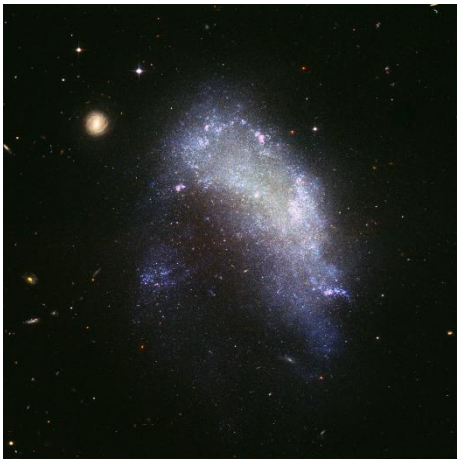

(d)

Fig. 1. The illustration of Hubble classification is present in Panel (a), and Panel (b) shows an example of an elliptical galaxy, with additional plots for a spiral galaxy and an irregular galaxy in Panel (c) and (d), respectively.

There are billions of galaxies in the Universe, and different galaxies have very diverse appearances. Edwin Hubble developed a galaxy morphology-based classification approach, dividing galaxies into spiral galaxies, elliptical galaxies, and irregular galaxies. It is based on the size of the central bulge and the texture of the cantilever, further subdivided spiral galaxies. Shown as Fig. 1, the luminosity distribution of elliptical galaxies is apparently smooth ellipses. Usually, they are massive galaxies in the universe. The proportion of gas and dust is relatively lower and contains many low-mass, aged stars. Meanwhile, the motion of stars shows irregular random motion produced by colliding and merging of low-mass galaxies.

On the other hand, spiral galaxies can be further subdivided into spiral galaxies with only spiral arms and barred spiral galaxies with central bar structures. A spiral galaxy is characterized by its rotating structure and disk shape, so also called a disk galaxy. A spiral galaxy usually hosts a central bulge with two or more spiral arms. The diameter of the bulge is generally smaller than the disk, but it contains most of the stellar mass in the galaxy. The bulge usually appears red in colors, which illustrate that it is mainly composed of long-lived low-mass stars. Within the bulges, there are also supermassive black holes in the center. The spiral arms are believed to originate from density waves in the stellar disks, where the majority of the star formation activities occur in the galaxies. As a result, the region is usually filled full of gas, dust, and young stars. The radiation from these young stars makes the spiral arms look brighter than anywhere else. Barred spiral galaxies are a special type of spiral galaxy characterized by an obvious bar structure. This bar structure is composed of stars, which move along a fixed orbit. Spiral arms extend from two sides, which is similar to normal spiral galaxies.

The morphology of irregular galaxies is relatively complex, and there is no obvious spinning also disk structure. Their stellar kinematics and dynamics are always influenced by strong interactions between two galaxies, like colliding and merging. These interactions can trigger star formation and also significantly modify the galaxy morphology.

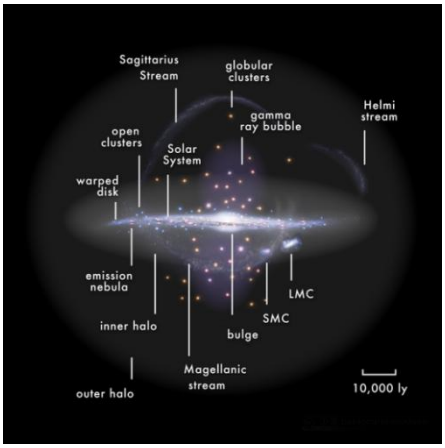

(a)

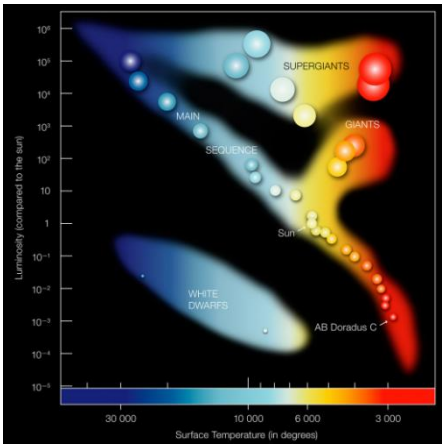

(b)

(c)

(d)

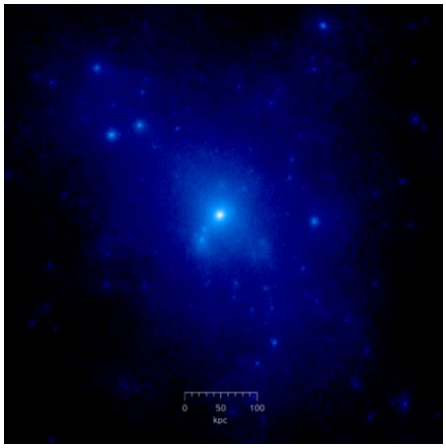

(e)

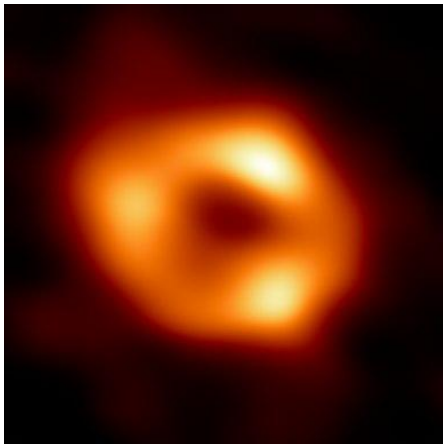

(f)

Fig. 2. Panel (a) shows the structure of the Milky Way, and Panel (b) describes the HR diagram of stars with diverse properties. An HST image of a globular cluster is present in Panel (c), and Panel (b) presents a JWST imaging of a giant molecular cloud. Panel (e) gives a snapshot of the dark matter halo in numeric simulations, and the observed image of the galactic supermassive blackhole via Event Horizon Telescope is given in Panel (f).

The galaxies are composed of stars, star clusters, interstellar medium, dark matter, and the supermassive black hole in the center. Stars are the dominant component of luminosity, typically numbering in the hundreds of billions. Stars are formed by the collapse of the giant molecular cloud in the universe under self-gravity. This process triggers nuclear fusion, thus emitting light and heat. As shown in Fig. 2, there are various categories of stars, including main-sequence stars, Red Giants Branch (RGB) stars, white dwarfs, neutron stars, and supernovae. The stellar life cycle dramatically varies, ranging from millions of years to tens of billions of years. In the final stage of its life cycle, stars undergo a series of changes, probably forming red giants, white dwarfs, and even black holes. Throughout these processes, heavy elements can be produced, further enriching the chemical abundances in the universe.

The star cluster typically contains a large number of stars in a small, dense group that can be categorized into globular clusters and open clusters. Globular clusters are dense clusters composed of hundreds of thousands to millions of stars located in the core or halo of a galaxy. Typically, these clusters are very old, even as old as the Universe, reflecting the earliest history of galaxy formation. Open clusters are generally located in the disks, formed by dozens to thousands of stars. These stars are usually young, indicating more recent

star formation activities in galaxies.

The interstellar medium consists of gas and dust dispersed in interstellar space. Interstellar gas is mainly composed of hydrogen and helium mixed with some heavy elements and is the main source of star formation. Interstellar dust is composed of solid-state materials formed via heavy elements, such as carbon, silicon, and so on, usually in the form of micron or nanometer particles, which scatter and absorb interstellar light, making distant stars and galaxies appear reddened.

There has been a supermassive black hole in the central region of the galaxy. The mass of these supermassive black holes can reach millions to billions of times the solar mass. Although it is difficult to detect black holes directly, we can infer their existence through their effects on the surrounding matter, for example, the accretion disk, which can emit strong radiation under high temperatures, forming AGN. Furthermore, the black hole can also influence the formation and evolution of galaxies.

C. Active Galactic Nuclei

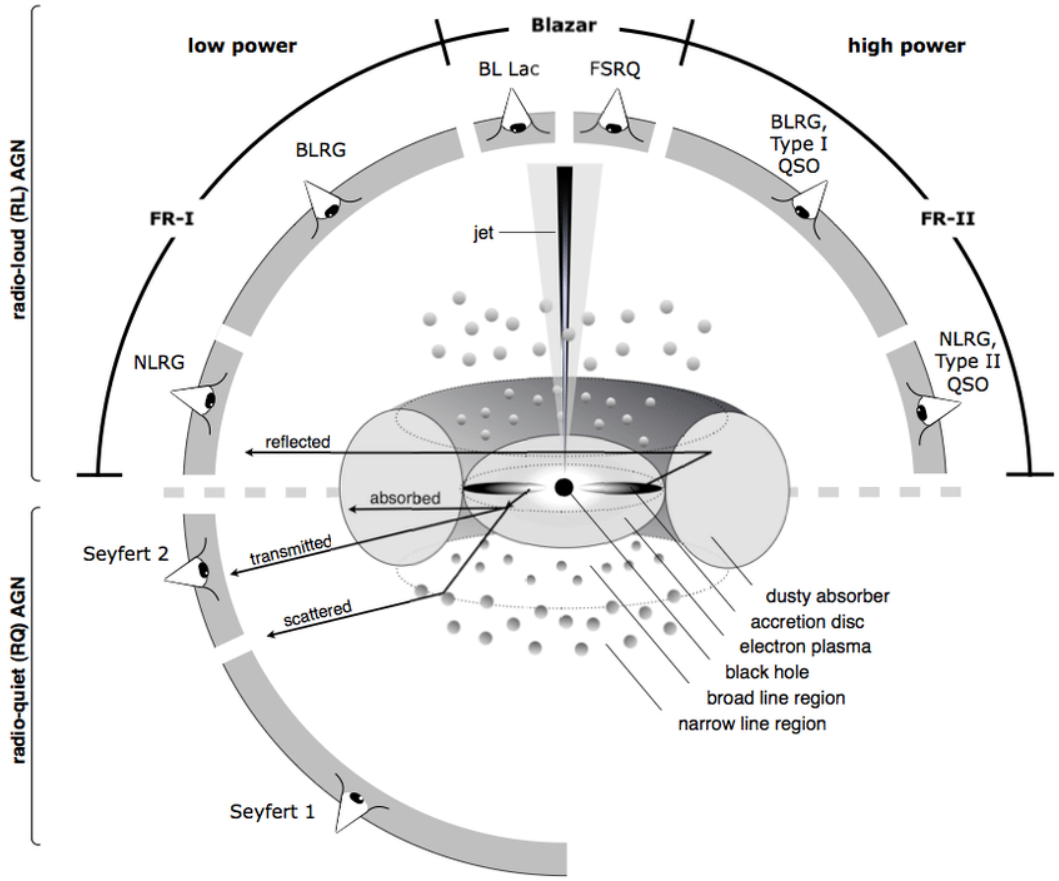

Fig. 3. Schematic representation of the unified model of AGN. From inside to outside, the basic structure is a supermassive black hole, an accretion disk, an accretion disk corona composed of high-temperature plasma, a broad emission line region, a dust torus, and a narrow emission line region. Different line-of-sight directions determine the corresponding physical properties and thus determine the observed types of AGNs.

Active Galactic Nuclei (AGNs) are bright objects at the center of galaxies. One of their distinctive features is the non-stellar radiation they emit, which is several orders of magnitude stronger than the radiation produced by ordinary galactic processes. This emission has unique spectral features that characterize the presence of an AGN.

Based on the observed properties, AGN can be broadly classified into different types, each with unique characteristics and radiation mechanisms, as shown in Fig. 3. A commonly used classification scheme divides AGNs into Seyfert galaxies and quasars. Seyfert galaxies are active galactic nuclei that are found in the galaxy relatively nearby, usually characterized by their emission lines in the spectrum. Depending on whether their spectra exist in broad emission lines, the Seyfert galaxies are further divided into Seyfert type I and Seyfert II. Quasars, in other words, are extremely bright, active galactic nuclei and are always associated with young, actively accretion supermassive black holes. Intense continuum radiation and prominent emission lines are major prominent features of quasars, however, not for Seyfert galaxies. Besides, Blazars belong to a special category of special active galactic nuclei. Its relativistic jets are directly pointed at the observer, causing highly gathered radiation. The flare sources are known as the transients in the electromagnetic spectrum, from radio waves to gamma rays. Another subclass is radio galaxies. It has strong radio radiation and is related to a focused jet. These jets that provide energy to supermassive black holes and accretion disks push the relativistic plasma to regions far from the core of AGN.

The structure of AGN is very complex, and its core is a supermassive black hole surrounded by an accretion disk. The gravity produced by supermassive black holes dominates the accretion process. The hot ionized plasma forms the

accretion disk; its inward spiral heats the disk to extremely high temperatures and emits strong radiation. The radiation appears in the board continuous spectrum and covers a wide range of wavelengths from radio to gamma.

Except for the accretion disk part, AGN also presents a strong relativistic particle jet and extends to large galactic scales. These jets are believed as emitted from the region close to the black hole and vertically to the accretion disk. The exact mechanism of the jet formation and acceleration is still under active investigation. Jet can emit radiation in every band in the spectrum, especially radio radiation. The AGN with visible jet called radio loud, in contrast, those who has no visible jet called radio quiet.

In the outer part of the accretion disk, there is a broad emission line region composed of high-temperature gas. This region is characterized by emission lines with line widths typically in the range of several thousand to tens of thousands of kilometers per second. There is a dust ring outside the broad emission line region, which is composed of gas and tiny dust grains. The existence of the dust ring can block the light from the central region. In contrast, the narrow emission line region is located far away and is mainly composed of gas obscured by the dust ring. The emission lines in this region are relatively narrow, with line widths typically in the range of a few hundred to a thousand kilometers per second. The narrow emission lines are mainly from the radiate recombination effect of the gas.

The unified model of AGN aims to explain the diversity of AGN properties by assuming a unified structure that appears to have different characteristics depending on the direction of the line of sight or the observer. According to this model, the observed variability of various types of AGN can be attributed to the orientation of their central parts with respect to the line of sight of the observer, as shown in Fig. 3. The dust torus, composed of a mixture of gas and dust particles, is thought to be responsible for obscuring the central region of AGN when we viewed from certain angles. When the dust torus is observed on the edge side, it will block the radiation from the broad line region, which accounts for the type-II AGNs. On the contrary, when a dust torus is observed from a face-on direction, we can directly detect the radiation in the accretion disk and broad line region; this is a characteristic of type I AGN.

Furthermore, this model can also illustrate the origin of blazers. In the model, blazers are described as an active galactic nucleus observed from a specific direction, where the jets closely aligned with our line of sight, causing observed extreme radiation and variability, leading to observed obvious radio radiation. In contrast, in radio-quiet active galactic nuclei, jets may be in different directions, causing radio radiation to blur and be less noticeable.

The unified model of AGNs has been widely supported by observational evidence and theoretical modeling. It provides a comprehensive framework for understanding the diversity properties and classification of AGN, successfully accounting for the observed variability in AGN spectra, emission lines, and other key properties by taking into account directional effects and the presence of dust torus. However, it should be noted that there are also some challenges and unresolved mysteries in the unified model. The geometry and characteristics of dust torus and the mechanism of jet formation and orientation are still active research areas. Additionally, this model does not completely explain all subclass and variations of AGN. Furthermore, other factors may influence the diversity of observation.

D. Weak Emission Line Quasars

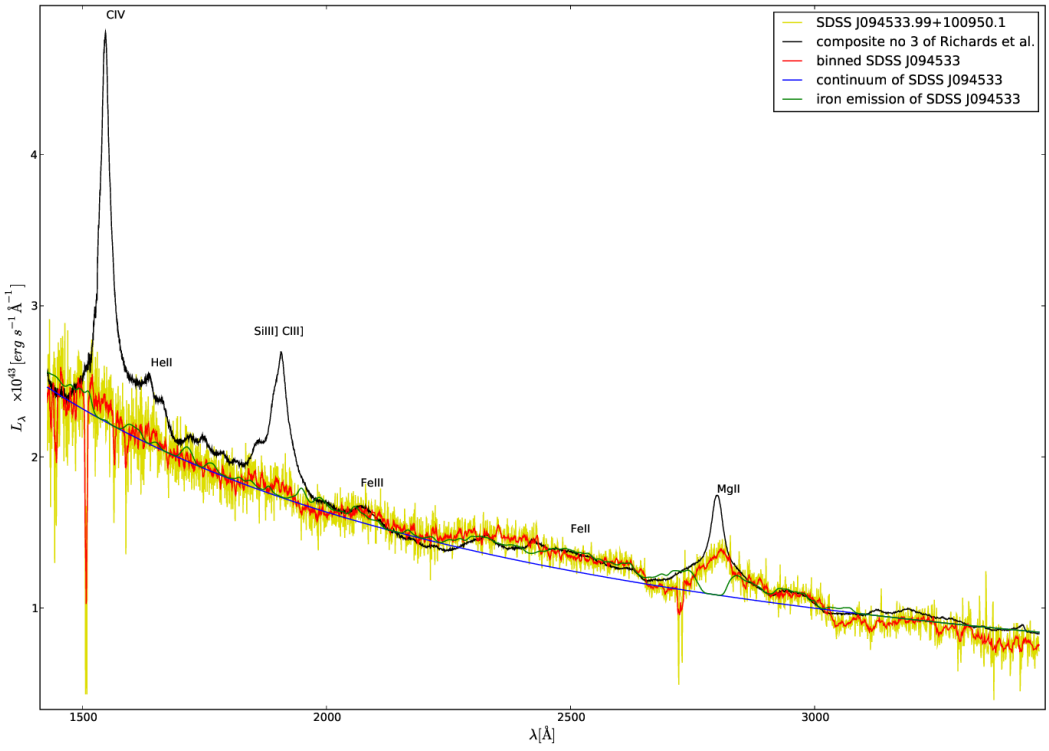

Fig. 4. Spectrum of weak emission line quasar SDSS J094533.99+100950.1 [1]. The black line in the Figure represents the average spectrum of normal emission line quasars; the red line indicates the detected signals; the yellow lines show the results after re-composition.

Weak Emission Line Quasars (WELQs) are a special type of quasars whose emission lines in their spectra are coherently weak relative to typical quasars [2]. These objects are characterized by lower equivalent widths of their emission lines, indicating fewer strong emission lines compared to typical quasars, and their typical spectral characteristics are shown in Fig. 4. The features of WELQs indicate several potential explanations for the observed weak emission lines in these objects. One possible explanation is the presence of an obscuring medium, such as a dust torus or dense gas cloud, partially or completely absorbing the broad emission-line region directly seen from our line of sight [3]. This absorption may lead to dilution of emission lines and eventually cause weak emission line features. The existence of absorbing material may indicate that when compared to normal emission line quasars, WELQs have different orientations or evolutionary stages. Another possible explanation has to do with the intrinsic properties of the central black hole. One hypothesis is that weak emission line quasars may be in a low accretion state. The low accretion rate leads to a weakening of the line intensity. It assumes that this condition may come from changes in the ionization structure or gas dynamics within the broad line region, leading to the weak emission line phenomenon observed in these objects [4]. Other possibilities are related to the physical conditions in the board line region. It also conjectures that weak emission line quasars may contain low-density or low-ionization gas in the broad line region. This may come from the changes in ionization structures or gas dynamics in the board line region caused by the low emission lines phenomenon observed in these objects [1]. In this work, we aim to study the weak emission line quasars with a large sample of data and to analyze the average energy spectrum distribution with multi-wavelength band data so as to understand their formation and evolution mechanisms.

II. Methodology

A. Selection of Sample Data

We are using the reduced catalogue from [5, 6], which contains 750414 quasars in total with subsequent analysis on the spectroscopy following the Sloan Digital Sky Survey (SDSS) fiducial data release. It spans over the range of redshift between $0 \leq z \leq 6$. It includes photometric data from the SDSS and spectroscopic measurements from the Baryonic acoustic Oscillation Spectroscopic Survey (BOSS). Observed wavelengths of emission lines of various elements such as Hydrogen, carbon, and oxygen; spectroscopic redshift, spectral flux density, equivalent width and the corresponding errors and the black hole mass M_{BH}; thermal luminosity L_{bol} inferred from the spectral data and other intrinsic physical properties of quasars. The flux density of spectral lines and the equivalent width and its corresponding errors. The black hole mass inferred from spectrum information M_{BH}, bolometric luminosity L_{bol} and other intrinsic physical properties of quasars. Moreover, this category also adds multi-band photometric data, including ultraviolet band Galaxy Evolution Explorer (GALEX) [7], the United Kingdom Infrared Telescope Deep Sky Survey (UKIDSS) [8], and wide-field survey in X-ray wavelengths and radio frequency.

First, we remove quasars with prominent Broad Absorption Line (BAL) features and systems with Damped Lyman Alpha (DLA) absorption characteristics to avoid the possible pollution to weak emit line quasars samples. Concretely, we reduced the initial quasar catalogue via setting BAL_PROB=0&CONF_DLA=0. On this basis, we choose Hα, Hβ, MGII, Lyα to perform a preliminary quasar screening. For spectroscopic detectors of SDSS and BOSS, the effective wavelength range is $380\mathrm{nm}<\lambda^{\mathrm{SDSS}}<920\mathrm{nm}$, $360\mathrm{nm}<\lambda^{\mathrm{BOSS}}<1040\mathrm{nm}$, therefore we can gain their observed redshift range as Table 1 shown. After this selection, we got 622821 quasars.

Table 1. The pivot wavelengths of four emission lines Hα, Hβ, MGII, Lyα. Afterwards, format listed the efficient redshift range $z_1^{\mathrm{SDSS}} < z^{\mathrm{SDSS}} < z_2^{\mathrm{SDSS}}$ an$z_1^{\mathrm{BOSS}} < z^{\mathrm{BOSS}} < z_2^{\mathrm{BOSS}}$d

Name	Hα	Hβ	MGII	Lyα
λ_0/nm	656.46	486.27	279.91	121.52
z_1^{SDSS}	−0.42	−0.22	0.36	2.13
z_2^{SDSS}	0.405	0.89	2.29	6.57
z_1^{BOSS}	−0.45	−0.26	0.29	1.96
z_2^{BOSS}	0.40	1.14	2.72	7.56

Next, our preliminary source selection strategy is as follows: we limit the total redshift range to $0.0 \leq z \leq 3.0$. Because when $z>3.0$, the number of quasars will be greatly reduced, and the luminosity distribution of the sample will be concentrated at the bright end, which will bring bias to the sample selection. At $0.0 \leq z^{\mathrm{SDSS}} < 0.41$ and $0.0 \leq z^{\mathrm{BOSS}} < 0.40$, we use the H$\alpha$ emission line to select the sample, a total of 24982 quasars; and at $0.41 \leq z^{\mathrm{SDSS}} < 0.89$ and $0.40 \leq z^{\mathrm{BOSS}} < 1.14$, although we already have MGII detections, we still choose to use Hβ. Because the equivalent width of Hβ is stronger than that of MGII. Therefore, we try to avoid the systematic bias introduced by the dark end of the luminosity distribution of celestial objects. Then there are 140,173 quasars in the range of $0.89 \leq z^{\mathrm{SDSS}} < 2.13$ and $1.14 \leq z^{\mathrm{BOSS}} < 1.96$. We use the MGII spectral line as the selected diagnostic and obtain a total of 337,067 quasars. Finally, in the range of $2.29 \leq z^{\mathrm{SDSS}} < 3.00$ and $1.96 \leq z^{\mathrm{BOSS}} < 3.00$, we use the Ly$\alpha$ spectral line as the selected diagnostic and obtain a total of 162,196 quasars. Based on this, we obtain the equivalent width distributions of the four emission lines as shown in Panel (a) of Fig. 5. Next, we limit the emission line intensity by selecting the minimum value 5% in the equivalent width distribution through the equivalent width distribution function, thereby obtaining candidates for weak emission line quasars. In part (b) of Fig. 5, the luminosity distribution is displayed in multiple colors, representing the different emission lines selected by the sample. We can find that the purple and blue solid lines representing the sample distributions selected by Hα and Hβ are systematically darker than the black solid line marking

the luminosity distribution of the entire quasar catalog. Therefore, it shows that there are many dim quasars in the samples selected by Hα and Hβ, rather than intrinsically weak emission lines, indicating that the dark end of the quasar luminosity function may be contaminated.

After all, we adjusted the source selection strategy. We adjust the total redshift range is $1.0 \leq z \leq 3.0$ to avoid a large number of the samples by a large number of low redshift quasars located at the faint end of the quasar luminosity distribution. Meanwhile, we limit the sample filtering at the use of two emitting lights MGII and Lyα, abandon to use Hα and Hβ. In this condition, in $1.0 \leq z^{SDSS} < 2.13$ and $1.0 \leq z^{BOSS} < 1.96$, we use MGII to screaming samples, and finally got 15333 quasars. In $2.13 \leq z^{SDSS} < 3.0$ and $1.96 \leq z^{BOSS} < 3.0$, we use Lyα to filter the samples, and finally obtained 8110 quasars. In total, we got 23443 quasars. Next, we divided the obtained weak emission line quasars candidates into four redshift ranges, $1.0<z<1.5$, $1.5<z<2.0$, $2.0<z<2.5$, $2.5<z<3.0$. As Fig. 6(a) shown, we can see in different redshift ranges, the weak emitting lines quasars candidates luminosity distribution represented by black line is approximately the same. Although in $2.0<z<3.0$, luminosity distribution entirely moves to luminous ends but will not cause a significant impact.

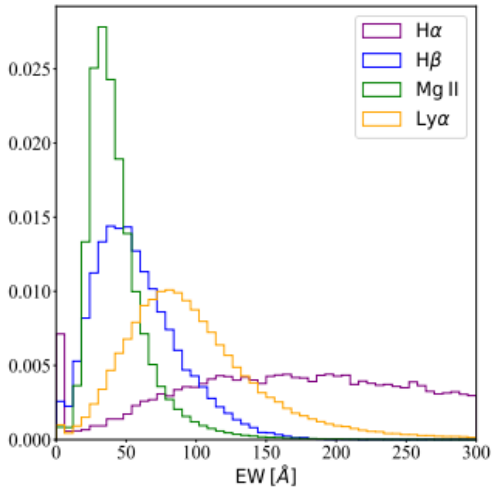

(a)

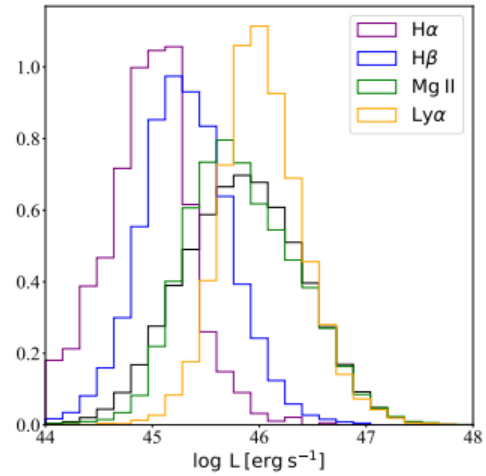

(b)

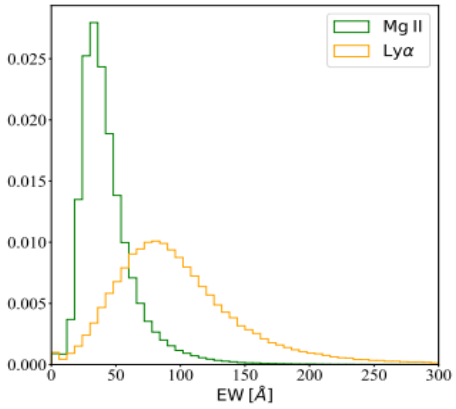

(c)

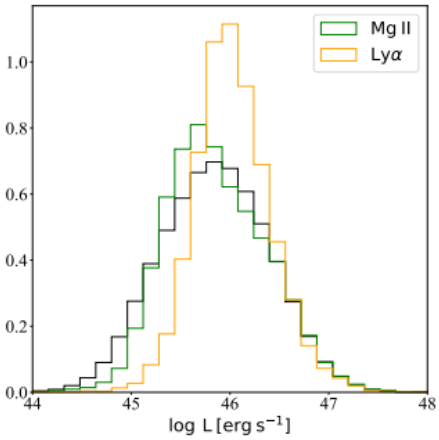

(d)

Fig. 5. (a) shows the equivalent width distribution of weak emission line quasar candidates obtained by screening the four emission lines Hα, Hβ, MGII, and Lyα. The purple, blue, green, and orange solid lines in the figure represent the results of sample screening based on Hα, Hβ; MGII; and Lyα, respectively; (b) shows the corresponding thermal luminosity distribution of weak emission line quasar candidates, and the black solid line is the overall luminosity distribution of all quasars; (c) shows the equivalent width distribution of weak emission line quasar candidates obtained by screening the two emission lines MGII and Lyα; (d) shows the corresponding thermal luminosity distribution of weak emission line quasar candidates. The black solid line is the overall luminosity distribution of all quasars.

After all, we have adjusted the source selection strategy and obtained the effective wavelengths of the SDSS bands, which are u band λ_U=354.3nm, g band λ_G=477.0nm, r band λ_R=623.1nm, i band λ_I=762.5nm, z band λ_Z=913.4nm. Specifically, we set GALEX_MATCH = 1, limiting that samples must contain the ultraviolet GALEX datasets, which have flux detections in two bands Far Ultraviolet (FUV) and Near Ultraviolet (NUV) with effective wavelengths of λ_{FUV}=153.86nm and λ_{NUV}=231.57nm. Next, after setting UKIDSS_MATCH = 1, we obtained UKIDSS photometric effective wavelength for band λ_Y=1.0305μm, band λ_J=1.2483μm, band λ_H=1.6313μm, band λ_K=2.2010μm. Adding in another band, like X-rays and radio information, will significantly reduce the target amount, so we do not include these additional selection criteria. After the restrictions of GALEX and UKIDSS, we obtained a total of 4554 quasars. In the four redshift ranges of $1.0<z<1.5$, $1.5<z<2.0$, $2.0<z<2.5$, and $2.5<z<3.0$, we obtained 1641, 1206, 1375, and 332 weak emission line quasars, respectively. The corresponding luminosity distribution is shown in (b) of Fig. 6. By adding multi-band restrictions, although the number of weak emission line quasar targets is reduced, it

does not significantly affect the luminosity distribution of the samples in different redshift ranges, so it will not cause deviations in the properties of the targets.

After a joint analysis of the multi-band data, we screen the celestial coordinates of the weak emission line quasar targets in Right Ascension (RA), Declination (DEC) and upload them to the Infrared Science Archive (IRSA) of the Infrared Processing and Analysis Center (IPAC) to obtain the corresponding scientific data. As Fig. 7 (a) shows, we use Wide-field Infrared Survey Explorer (WISE) point source catalogue. We cross-certify a sample of weak emission-line quasars within an angular distance of 6″. Thus, we can determine whether there is a corresponding WISE data measurement and obtain the corresponding point source magnitude measurement with the effective wavelength of band λ_{W1}=3.4μm, band λ_{W2}=4.6μm, band, band λ_{W3}=12.0μm, and band λ_{W4}=22.0μm. With the obtained WISE data tables, the weak emission-line quasar sample is constrained to have magnitude data in all WISE bands. After this screening, we end up with a collection of 3719 quasars. In four red draft ranges: $1.0<z<1.5$, $1.5<z<2.0$, $2.0<z<2.5$, $2.5<z<3.0$, we obtain 1483, 1018, 1014, 204 weak emission line quasars respectively. And the corresponding luminosity distribution is shown in Fig. 6(c). The number of weak emission line quasars is further reduced, and the quasars in $2.5<z<3.0$ show a systematic shift to the bright end of the luminosity distribution, which limits the subsequent comparative analysis.

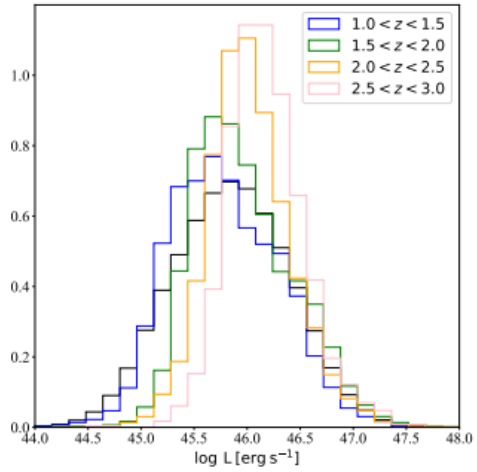

(a)

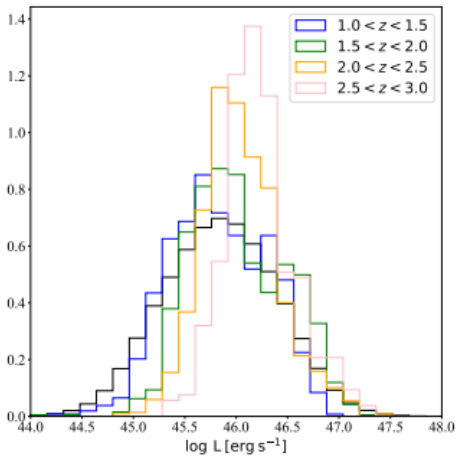

(b)

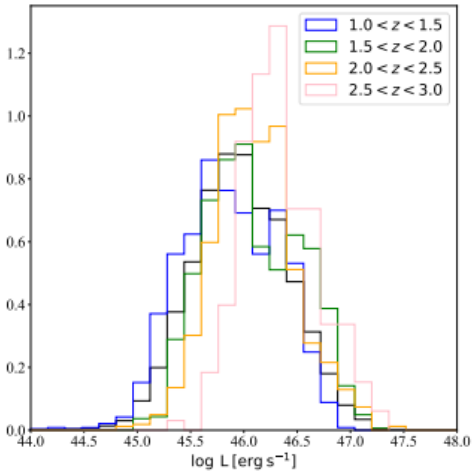

(c)

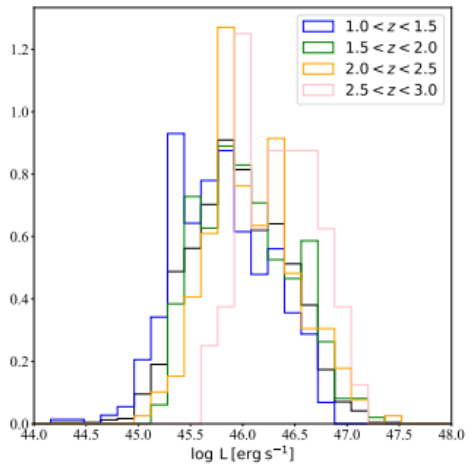

(d)

Fig. 6. The luminosity distribution of weak emission line quasar samples in various stages in different redshift ranges. The blue solid line, green solid line, orange solid line, and pink solid line represent the four redshift ranges of $1.0<z<1.5$, $1.5<z<2.0$, $2.0<z<2.5$, and $2.5<z<3.0$, respectively, while the black solid line is the overall luminosity distribution of all quasars.

Furthermore, we use the IRSA database to obtain the far-infrared image data by Spectral and Photo-metric Imaging Receiver (SPIRE) from the Herschel Space Telescope, as shown in Fig. 7(b). Here, we set the angle distance to retrieve the image data to 0.1˚. The SPIRE image data contains three bands with effective wavelengths of 250μm, 350μm and 500μm. And, we cut off the original SPIRE images with size 10'×10' stamps and confirm that the percentage of pixels measured in the captured image is greater than 75% to exclude the weak emission line quasars with missing image data or low data quality. After careful screening of the image data, we have obtained a final sample of 1062 weak emission line quasars in the four Redshift ranges of $1.0<z<1.5$, $1.5<z<2.0$, $2.0<z<2.5$, $2.5<z<3.0$, and our sample numbers are 457, 309, 246, 50, The corresponding luminosity distribution is shown in Fig. 6 (d). The number of quasars within $2.5<z<3.0$ is less than 100, which will affect the representative of the sample, and its obvious systematic shift to the bright end of the luminosity distribution will increase the limitation of the applicable type for subsequent studies. It is necessary to compare with the normal emission line quasars at the bright end of the luminosity distribution function in order to understand their physical properties better.

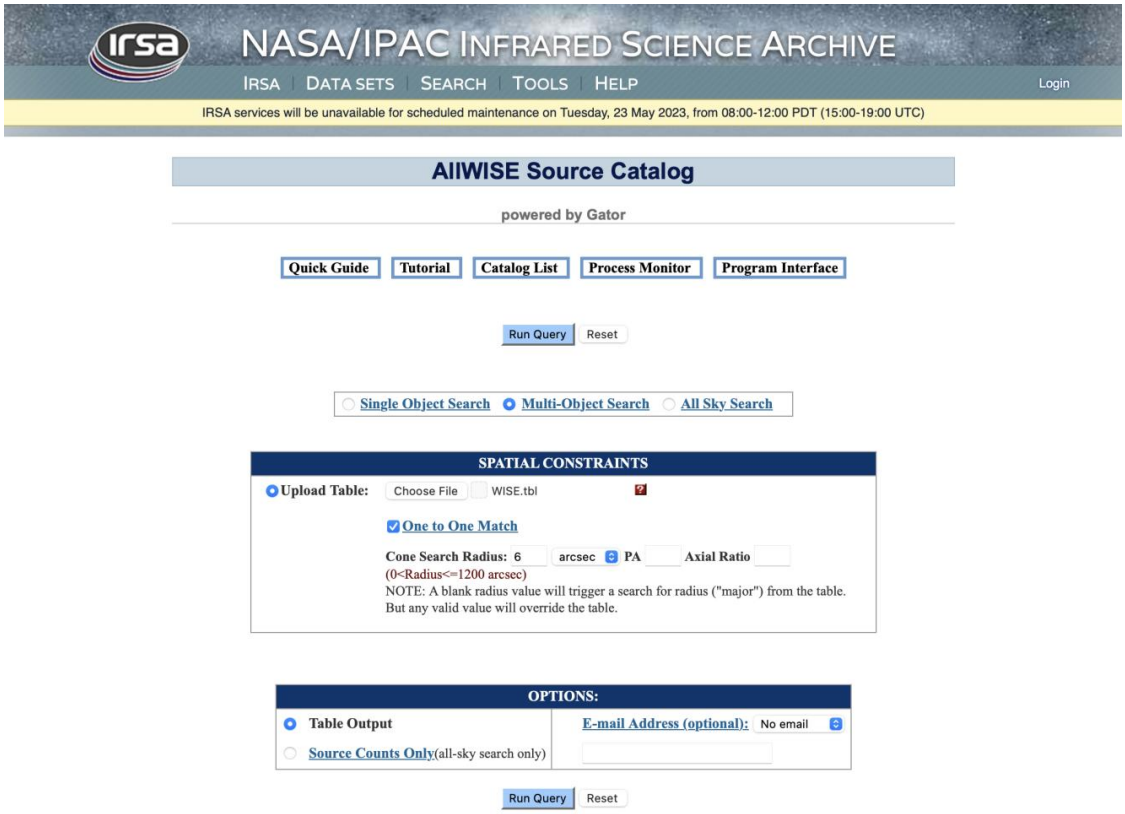

(a)

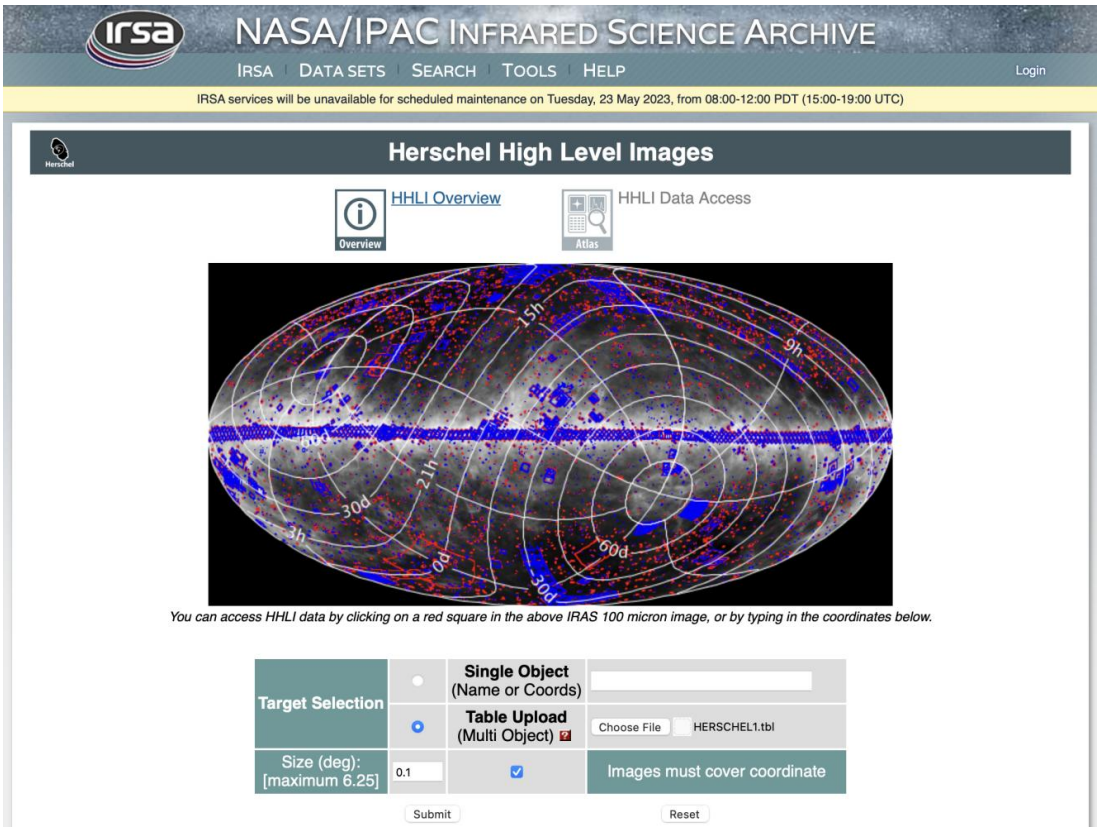

(b)

Fig. 7. Screenshots from the Infrared Science Database on the IRSA official website: (a) shows the cross-verification with the WISE all-sky point source catalog; (b) shows the acquisition with SPIRE image data.

B. Image Analysis and Stacking

After selecting quasars and the inspection of the quality of SPIRE far-infrared image data, we finally obtained 623, 400, 345, 100 images with angular size 10'×10' in four red draft ranges: $1.0<z<1.5$, $1.5<z<2.0$, $2.0<z<2.5$, $2.5<z<3.0$. The effective observation wavelengths of SPIRE are 250μm, 350μm and 500μm, and the pixel sizes of each image are 101pixel×101pixel, 73pixel×73pixel and 51pixel×51pixel. For each science picture, we have its corresponding

uncertainty map, which quantifies the statistical and systematic errors. An example of a far-infrared image is shown in Fig. 8, we can see that due to the relatively high noise level of a single far-infrared image σ~0.05Jy/Beam, the Signal Noise Ratio (SNR) of the image does not reach a statistically significant detection. Thus, for a single object, we cannot accurately obtain its true far-infrared radiation intensity.

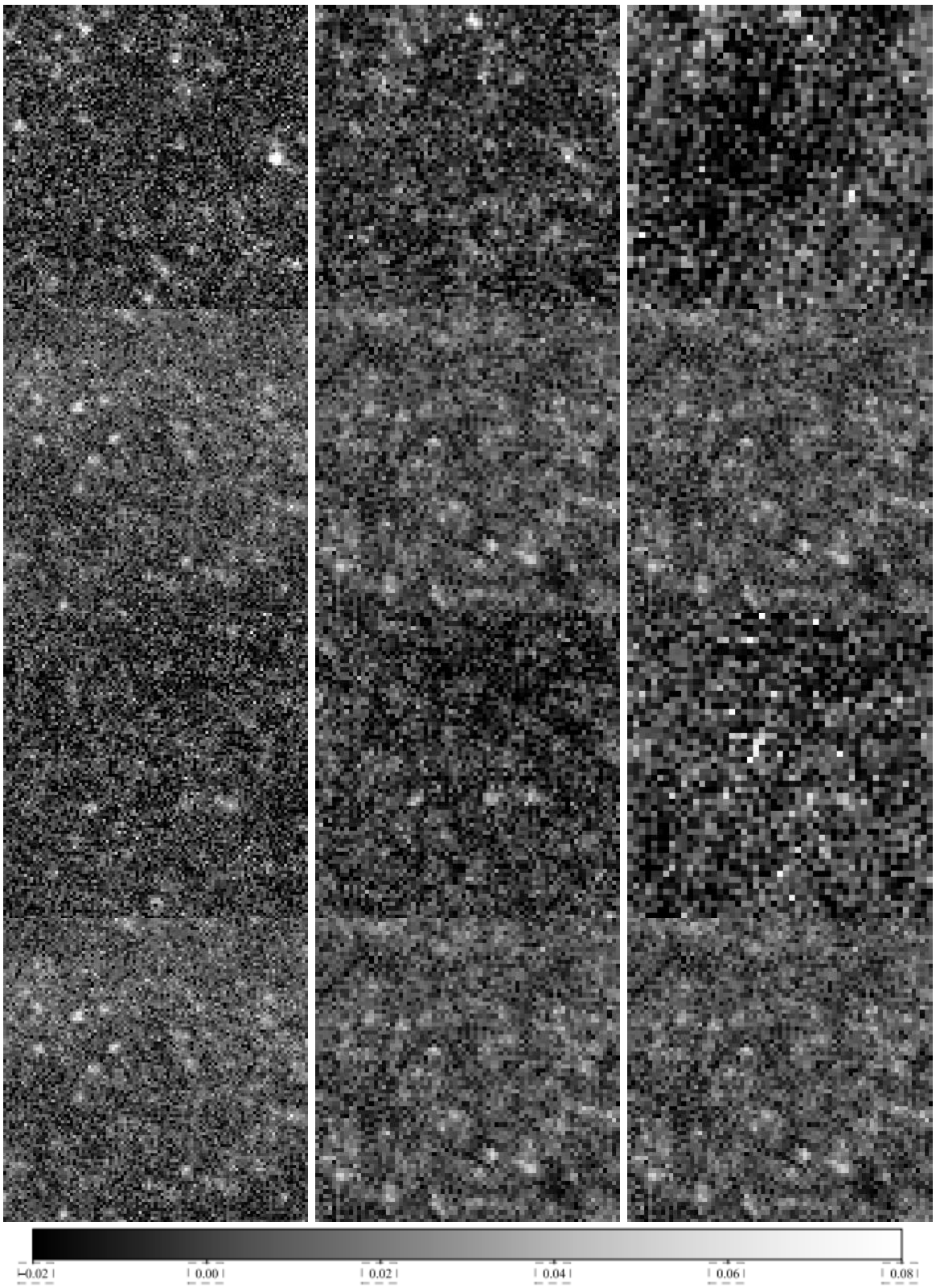

Fig. 8. An example of a SPIRE far-infrared image of a single sample. From left to right, there are three bands with effective observation wavelengths of 250μm, 350μm, and 500μm. From top to bottom, there are four redshift ranges of $1.0<z<1.5$, $1.5<z<2.0$, $2.0<z<2.5$, and $2.5<z<3.0$.

To obtain statistically significant average estimate, we ran a total of 5000 random simulations. In each random simulation, we randomly choose a sample of weak emission-line quasars in different redshift ranges. It is assumed that the value of each pixel on all image satisfies a Gaussian distribution with its measured value as the average value and the uncertainty as the standard deviation. A random number is generated to obtain a random map. And via using

the median map as the average of each random simulation, we avoid the influence of the image data of extreme samples on the final superposition results. Finally, the average of all the resulting median pictures is taken as the final stacked image. The standard deviation of the resulting median image is the statistical errors. The stacked images in the different redshift ranges are shown in Fig. 9. Due to the stacking of a large number of image datasets, the random error level at the edge of the picture is clearly reduced by σ∼0.005Jy/Beam. On the other hand, the signal strength in the centre of the picture is not significantly reduced due to the superposition of a large number of pictures. As a result, we obtain a higher signal-to-noise ratio, raising ∼10-20 times than a single image, which allows accurate and statistically significant measurements to be made on the stacked images, resulting in an average far-infrared flux density.

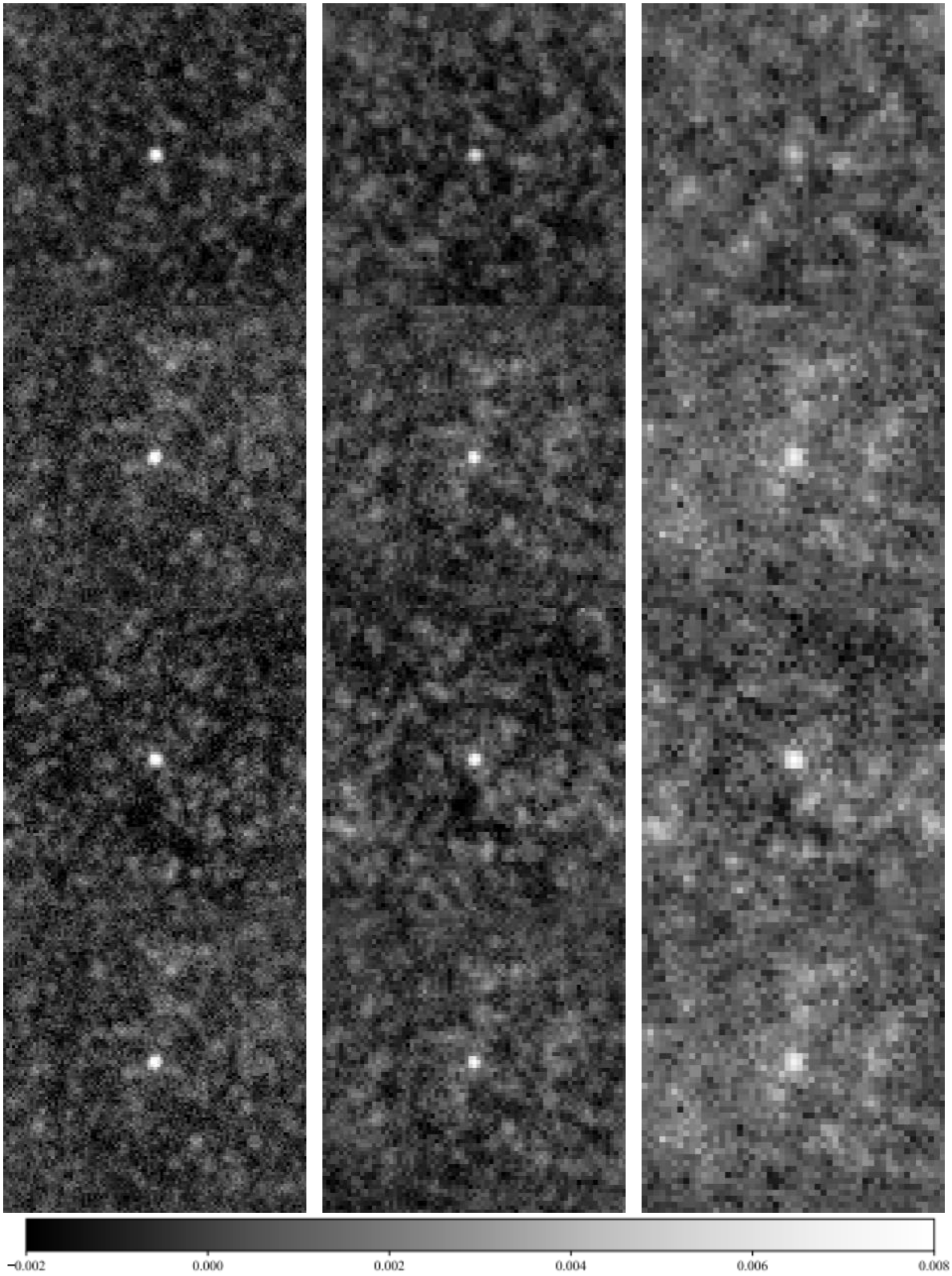

Fig. 9. SPIRE far-infrared superposition images of samples in different redshift ranges. From left to right, there are three bands with effective observation wavelengths of 250μm, 350μm, and 500μm. From top to bottom, there are four redshift ranges of $1.0<z<1.5$, $1.5<z<2.0$, $2.0<z<2.5$, and $2.5<z<3.0$.

C. Energy Spectrum Distribution Function

To obtain the multi-band Spectral Energy Distributions (SEDs), we uniformly correct the apparent flux densities for Milky Way dust extinction. Based on the dust absorption curve in reference [9], we use the color index $E(B\text{-}V)$, and hypothesis R_V=3.1, to obtain the corresponding dust extinction, so as to correct the intrinsic flux density.

For the WISE data in the mid-infrared band, we read the cross-certified W1 band, W2 band, W3 band, and W4 band apparent magnitudes obtained from the Infrared Science Database. From reference [10], we know that the standard zero-point fluence density for the four bands of WISE is $f^*_{\nu,\mathrm{W1}} = 306.68\mathrm{Jy}$, $f^*_{\nu,\mathrm{W2}} = 170.66\mathrm{Jy}$, $f^*_{\nu,\mathrm{W3}} = 29.04\mathrm{Jy}$, $f^*_{\nu,\mathrm{W4}} = 8.284\mathrm{Jy}$. In addition, the spectral index corresponding to the average WISE band flux density we obtained is $f_\nu \propto \nu^{-3}$. Therefore, our actual zero-point flux density needs to be corrected accordingly. For the correction factors corresponding to the four bands using the information on zero-point flux density, we can use the following formula to convert the WISE apparent magnitude into the corresponding flux density.

$$f_{\nu,X} = \frac{f^*_{\nu,X}}{\mathrm{h}_X} 10^{-0.4 m_X} \tag{10}$$

After obtaining the UV, optical, near-infrared and mid-infrared flux densities of a single weak emission-line quasar, it is necessary to get the average flux densities of the sample corresponding to different redshift ranges. Similarly, we have performed 5000 random simulations, and in each random simulation, we randomly sampled the weak emission line quasar samples in different redshift ranges. It is assumed that the flux density of all bands meets the Gaussian distribution with its measured value as the average value and the uncertainty as the standard deviation. The random number is generated to obtain the Gaussian random flow density, and the median flow density is obtained. The average of the resulting median flow densities is taken as the final sample average flow density. The standard deviation of the resulting median flow density is the statistical error of the sample mean flow density.

For SPIRE far-infrared images with different redshift ranges, we performed aperture photometry analysis. First, according to [11], for the three bands with effective wavelengths of 250μm，350μm and 500μm, the beam area (Beam Area) with SPIRE is $\Omega_{250\mu\mathrm{m}}$=465.35 arcsec^2, $\Omega_{350\mu\mathrm{m}}$=831.27 arcsec^2, $\Omega_{500\mu\mathrm{m}}$= 1804.31arcsec^2, we corrected the units of image data from Jy/Beam to Jy/pixel. We then chose the photometric aperture to be a circular aperture with a diameter of 6 pixel pixels. The corresponding angular diameters are $\theta_{250\mu\mathrm{m}}$=36″, $\theta_{350\mu\mathrm{m}}$=50″ and $\theta_{500\mu\mathrm{m}}$=72″. At the same time, we use the Full Width Half Maximum (FWHM) of the point source spread function (PSF) of the SPIRE far-infrared image in [12], with $\mathrm{FWHM}_{250\mu\mathrm{m}}$=18″, $\mathrm{FWHM}_{350\mu\mathrm{m}}$=25″, $\mathrm{FWHM}_{500\mu\mathrm{m}}$=36″. Moreover, under the assumption of two-dimensional Gaussian point source diffusion distribution, we have carried out the aperture correction. Finally, the average SPIRE far-infrared flux density of different redshift ranges is obtained.

So far, we have measured the flux density in the UV, optical, near-infrared, middle infrared and far infrared bands. Then, we will explore the radiation energy distribution of weak emission line quasars in different frequency bands through the detailed analysis of their SEDs so as to understand their formation and evolution.

III. Results and Discussions

A. Scientific Results

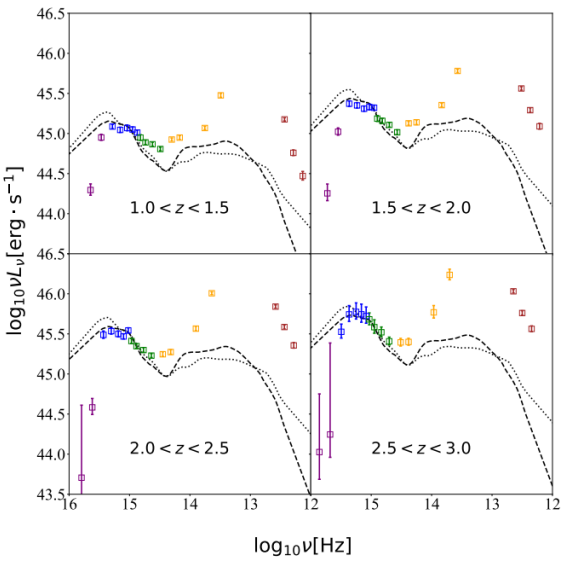

Fig. 10. 1.0<z<1.5, 1.5<z<2.0, 2.0<z<2.5, 2.5<z<3.0 are average energy spectrum distribution functions in four Redshift ranges. The vertical axis is logνL_ν [erg · s^{-1}], and the horizontal axis is logν[Hz], The purple squares, blue squares, green squares, orange squares, and brown squares represent the spectral distributions in the ultraviolet, optical, near-infrared, mid-infrared, and far-infrared, respectively. The corresponding statistical errors are given by the corresponding gray error bars. The black dashed and dotted lines represent the average spectral distribution function templates of radio-quiet and active normal emission line quasars from [13].

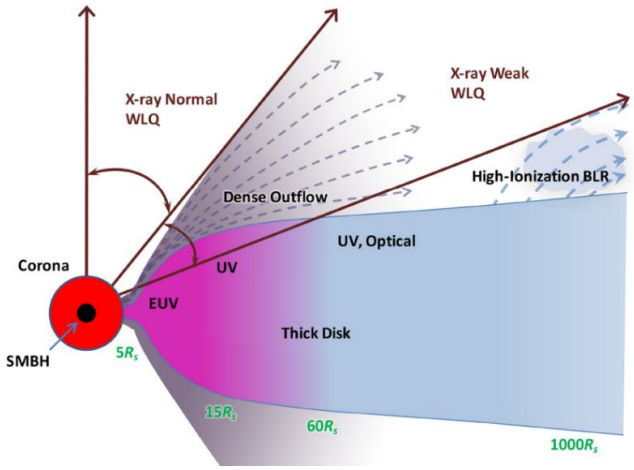

Fig. 11. The accretion disk wind model of the structure formation in weak emission line quasars in reference [14].

The observed frequencies are corrected to the rest frequencies according to the average Redshift of 1.27, 1.73, 2.19, 2.69, we adjust out observation frequency to rest frequency $\nu_0=\nu(1+z)$. Using the Planck satellite cosmological model result [15], we calculate the average luminosity distance d_L are 9090 Mpc, 13307 Mpc, 17802 Mpc, 22865 Mpc. Thus, we can obtain the monochromatic luminosity in the rest reference frame, whose calculation is given by the following formula.

$$L_{\nu_0=\nu(1+z)} = \frac{4\pi f_\nu d_L^2}{1+z} \tag{11}$$

The spectral energy distribution function in different

Redshift ranges is shown as Fig. 10. Here, we generalised a reference [13] in logν/Hz=15 about the average spectral energy distribution function of radio-quiet and radio-loud normal emission line quasars and the average spectral energy in observed weak emission line quasars to do research and compare.

In the rest wavelength ultraviolet band 15.5≤logν/Hz<16.0, here, the radiation energy mainly originates from the conversion of gravity energy that the accretion disk secretes surrounding substances. We find that the value of the ultraviolet band is significantly lower than the corresponding average template of normal emission line quasars, indicating that a considerable proportion of accretion disk radiation is absorbed by dust or gas. There are two primary sources of dusk and gas in quasars: the dust ring in the periphery of the dust ring of the accretion disk. It may illustrate that weak emitting lines quasars have relatively massive dust rings or greater masses of dust and gas in host galaxies, producing significant absorption to accretion disk in weak emitting lines quasars. Due to the lack of physical information on the absorption properties of dust and gas in quasars and host galaxies, we can not eliminate this effect for the time being.

In the rest wavelength optical band 15.0≤logν/Hz<15.5, the energy spectrum distribution of weak emission line quasars is similar to that of normal emission line quasars. It shows that the accretion disk properties of weak emission line quasars are not significantly different from those of normal emission line quasars. However, in the near-infrared band 14.5≤logν/Hz<15.0, there is also a component of host galaxies based on the non-thermal emission of quasars. This indicates that weak emission line quasars may have a strong component of stellar radiation from their host galaxies. This suggests that their host galaxies may be massive galaxies with relatively bright stellar radiation superimposed on the quasar radiation.

In the near mid-infrared band of rest wavelength 14.0≤logν/Hz<14.5, the radiation energy in quasars is mainly from the black body radiation by hot dust in the dust ring (500≲T≲1000), we observe that the dust ring component of weak emission line quasars is slightly higher than that of normal emission line quasars. There is no significant difference in the order of magnitude. It can be considered that the dust ring properties of weak emission line quasars are not significantly different from those of normal emission line quasars.

The most significant difference between weak emission line quasars and normal emission line quasars comes from the range of 13.0≤logν/Hz<14.0 at the far end of the mid-infrared band, where we find that the emission increases significantly, about ~5-10 times that of the template emission, and we also see that in the far-infrared band 12.0≤logν/Hz<13.0. The dust emission from star formation regions heated by star formation activity in the host galaxy dominated here is also significantly higher than the template by a factor of about 5-10. Thus, we assume it may be that the cold dust emission 50≲T≲100 in the host galaxy is too strong and much greater than the thermal radiation energy in the quasar dust ring so that the host galaxy component dominates the emission at the far end of the mid-infrared band. In addition, we also find that the spectral slope of the far-infrared emission is $L_\nu \propto \nu^{-2}$, indicating that there is a relatively steep emission spectrum here, which is closer to the spectral distribution function of the radio-quiet normal emission line quasars represented by the black dotted line in Fig. 10. Therefore, we infer that the average radioactivity of weak emission line quasars is generally weak, indicating that the far-infrared radiation is dominated by the dust radiation heated by the star formation activity of the host galaxy, and there is no contribution from the radio radiation.

Therefore, the above results show that the far-infrared band luminosity of weak emission line quasars is about ~5-10 stronger than that of normal discovery line quasars, and the far-infrared radiation is dominated by the black body radiation of cold dust in the host galaxy, which is heated by high-energy photons produced by massive stars in the star-forming region. These indicate that the host galaxies of weak emission line quasars have a considerable proportion of massive young stars, and the star formation activity is very active, which is likely to be in the stage of starburst formation. At this stage, a large number of stars formed in host galaxies in a fairly short cosmic time. According to the classical theory that galaxy formation and evolution, the special formation stage of the galaxy may caused by several different factors. The primary reason is that the galaxy is being the early stage of formation. Therefore there's a large amount of cold gas to accomplish star formation. Or, the galaxy had undergone a major merge with another same-mass galaxy to obtain extra cold gas supply, to lead further the galaxy eruption, leading to extremely active star formation. Here, we can exclude a minor merger scenario about a massive galaxy accretion and engulfing a smaller galaxy. In this situation, the significant mass disparity and other complex baryonic processes will not raise the proportion of cold gas to form a star, just bring corresponding mass and scale increase. Under the early galaxy major merge hypothesis, no matter which cases, all illustrate that weak emitting lines quasars' supermassive black hole should be triggered within a short cosmic time. Therefore, AGN should be in the early stage of evolution. Based on theoretical model in reference [14, 16], as shown in Fig. 11, the formation of outer structures of quasars requires the accretion disk wind to transport ionised gas to periphery of accretion disk, thus in the early stage of AGN evolution, the board-line and narrow-line region of quasars are not completely formed, leading the equivalent width of emission lines in quasars is significantly weaker than normal emission line quasars. This theory is are same as the significantly strengthened far-infrared radiation that we observed. Besides, in other weak emitting lines quasars, we also observed Strong star formation activities. As reference [17] shown. Hence, we believe that the co-evolution model of AGN and starburst galaxies is the physical origin of weak emission line quasars.

B. Summary and Outlook

The main goal of this study is to select a relatively complete sample of weak line emission quasars by using the large sample of the SDSS quasar catalogue so as to study the relationship between dust emission and star formation of weak line emission quasars and their host galaxies. Weak emission line quasar candidates are selected by using the equivalent widths of Lyα and MGII emission lines and by restricting their multi-band point source photometric data in

the ultraviolet GALEX, near-infrared UKIDSS, mid-infrared WISE and high-quality image information in the far-infrared SPIRE database. After that, through multiple random simulations and stacking analysis, we finally obtain the average energy spectral distribution function of weak emission line quasars in the four Redshift ranges of $1.0<z<1.5$, $1.5<z<2.0$, $2.0<z<2.5$, $2.5<z<3.0$. It is found that the far-infrared luminosity of quasars is ~5-10 times that of normal emission line quasars, indicating that the dust radiation of the host galaxies of weak emission line quasars is very strong, further indicating that they have intense star formation activity. This suggests that the host galaxies of weak emission line quasars are in the early stage of galaxy formation and evolution. According to the accretion disk wind model of quasar structure formation, we consider that the structure of the emission line region of the weak emission line quasar has not been fully formed, and finally explain the source of the weak emission line of this type of quasar.

However, due to the lack of all-sky multi-band data of quasars, the number of weak emission line quasars is limited. For example, the number of samples is limited by the W3 and W4 flux detection of WISE and the scarcity of quasars with high-quality far-infrared images. In the future, we can stack and analyse the near-infrared, mid-infrared, far-infrared, and radio image data of the whole sky, break through the restriction of the flux detection condition of a single sample on the number of quasars, and obtain a complete sample of weak emission line quasars. In addition, the next generation of spectroscopic surveys will obtain spectral line information of more than 1 billion distant galaxies. It will obtain unprecedented high-quality research data on quasars and weak emission line quasars. At the same time, more large-field multi-band photometric surveys in the future will bring about the explosive growth of high-quality image data throughout the day. At that time, we will have the opportunity to deeply understand the physical mechanism of the formation of weak emission line quasars and their role in the formation and evolution of galaxies.

Conflict of Interest

The author declares no conflict of interest.

Acknowledgment

I deeply appreciate Dr. Zhang for his guidance and assistance. I would also like to express my appreciation to the Sloan Digital Sky Survey (SDSS) and the Herschel Space Observatory for providing high precision resources that were greatly helpful in this research.

References

[1] Hryniewicz *et al.* "SDSS J094533.99+100950.1-the remarkable weak emission line quasar," *Monthly Notices of the Royal Astronomical Society*, vol. 404, no. 4, pp. 2028–2036, 2010.

[2] D. Stanic *et al.*, "High-redshift SDSS quasars with weak emission lines," *The Astrophysical Journal*, vol. 699, no. 1, pp. 782–799, 2009.

[3] Shemmer *et al.,* "Weak emission-line quasars in the context of a modified Baldwin effect," *The Astrophysical Journal*, vol. 805, no. 124, p. 8, 2015.

[4] Niko–lajuk *et al.*, "The environment of weak emission-line quasars," *Monthly Notices of the Royal Astronomical Society*, vol. 420, no. 3, pp. 2518–2525, 2012.

[5] Lyke *et al.*, "The Sloan digital sky survey quasar catalog: Sixteenth data re-lease," *The Astrophysical Journal Supplement Series*, vol. 250, no. 8, pp. 24–24, 2020.

[6] Wu *et al.*, "A catalog of quasar properties from Sloan digital sky survey data re-lease 16," *The Astrophysical Journal Supplement Series*, vol. 263, no. 42, p. 12, 2015.

[7] Martin *et al*., "The galaxy evolution explorer: A space ultraviolet survey mission," *The Astrophysical Journal*, vol. 619, no. 1, pp. L1–L6, 2005.

[8] Warren *et al.*, "The United Kingdom infrared telescope infrared deep sky survey first data release," *Monthly Notices of the Royal Astronomical Society*, vol. 375, no. 1, pp. 213–226, 2007.

[9] Fitzpatrick & Massa, "An analysis of the shapes of interstellar extinction curves. V. the IR-through-UV curve morphology," *The Astrophysical Journal*, vol. 663, no. 1, pp. 320–341, 2007.

[10] Wright *et al.*, "The Wide-field Infrared Survey Explorer (WISE): Mission description and initial on-orbit performance," *The Astronomical Journal*, vol. 140, no. 6, pp. 1868–1881, 2010.

[11] Griffin *et al.*, "The herschel-SPIRE instrument and its in-flight performance," *Astronomy and Astrophysics*, vol. 518, no. L3, p. 7, 2009.

[12] Swinyard *et al.*, "In flight calibration of the Herschel-SPIRE instrument," *Astronomy and Astrophysics*, vol. 518, no. L4, p. 6, 2009.

[13] Elvis *et al*., "Atlas of quasar energy distributions," *Astrophysical Journal Supplement*, vol. 95, p. 1, 1994.

[14] Ni *et al.*, "Connecting the X-ray properties of weak-line and typical quasars: testing for a geometrically thick accretion disk," *Monthly Notices of the Royal Astronomical Society*, vol. 480, no. 4, pp. 5184–5202, 2018.

[15] P. Collaboration *et al.*, "Planck 2018 results. I. Overview and the cosmological legacy of Planck," *Astronomy and Astrophysics*, vol. 641, no. A1, pp. 56–56, 2012.

[16] Luo *et al.*, "X-ray insights into the nature of PHL 1811 analogs and weak emission- line quasars: Unification with a geometrically thick accretion disk?" *The Astrophysical Journal*, vol. 805, no. 122, pp. 25–25, 2015.

[17] I. T. Andika et al., "Probing the nature of high-redshift weak emission line quasars: A young quasar with a Starburst host galaxy," *The Astrophysical Journal*, vol. 903, no. 1, p. 34, 2020.